Seismic evidence for a chemical heterogeneity in the midmantle: A strong and slightly dipping seismic reflector beneath the Mariana subduction zone

Fenglin Niu

Department of Earth Science, Rice University, Houston, Texas, USA

Hitoshi Kawakatsu and Yoshio Fukao

Earthquake Research Institute, University of Tokyo, Tokyo, Japan

[1]   A clear later phase $\sim$80 s after the direct P wave is observed in most of individual seismograms recorded by a short-period seismometer network in Japan (J-array) from a cluster of deep earthquakes that occurred at the northern Mariana subduction zone. This phase (1) shows a P wave particle motion, (2) arrives later from earthquakes with shallower focal depths, (3) has a steeper incident angle than that of P wave, and (4) shows a deviation of a few degrees in the arrival azimuth from that of P wave. We interpret it as an S-to-P converted wave which takes off downward from the source and is reflected at a velocity discontinuity (reflector) below the earthquakes. Travel time inversion shows that the seismic reflector dips southwest by $\sim$20° at 24.25°N, 144.75°E, and at a depth of 1115 km with a lateral extension at least 100×100 km. The location corresponds to the lower edge of a high-velocity anomaly in global tomographic models. Amplitude and waveform analyses suggest a decrease of S wave velocity by 2–6% and an increase of density by 2–9% within the reflector. There is almost no difference in P wave velocity (<1%) between the reflector and the surrounding mantle. The estimated thickness of the reflector is $\sim$12 km. These observations indicate that the observed seismic structure is more likely to be a chemical reservoir rather than a purely thermal anomaly. The seismic reflector might be a piece of subducted oceanic crust, as suggested by a previous study. It also could be related to the break down of the D phase of dense hydrous magnesium silicates at midmantle pressure condition reported by recent mineral physics studies. Both scenarios imply that mechanical/chemical segregation might occur within the subducted slab at midmantle condition.   *INDEX TERMS:* 7203 Seismology: Body wave propagation; 7207 Seismology: Core and mantle; 7260 Seismology: Theory and modeling; 8162 Tectonophysics: Rheology—mantle; 9355 Information Related to Geographic Region: Pacific Ocean; *KEYWORDS:* S-P reflection, seismic reflectors, midmantle, Mariana subduction zone, chemical heterogeneities

1. Introduction

[2] Many studies suggest that the lowermost several hundreds of kilometers (D″ layer) is very complicated and heterogeneous in terms of seismic structures [e.g., *Cleary and Haddon*, 1972; *Garnero and Helmberger*, 1995; *Mori and Helmberger*, 1995; *Kendall and Silver*, 1996; *Lay et al.*, 1998; *Wysession el al.*, 1999; *Wen*, 2001; *Niu and Wen*, 2001]. Both chemical and thermal processes have probably been involved in producing the structures [e.g., *Garnero and Helmberger*, 1995; *Mori and Helmberger*, 1995; *Kendall and Silver*, 1996; *Lay et al.*, 1998; *Wysession el*

al., 1999; *Wen*, 2001]. On the other hand, seismic signatures of heterogeneities in the lower mantle above the D″ layer (middle mantle) generally appear to be more subtle than the upper mantle. While several recent geodynamic models have proposed a compositional boundary in the middle mantle [*Kellogg et al.*, 1999; *van der Hilst and Karason*, 1999; *Davaille*, 1999; *Tackley*, 2000], detecting these chemical anomalies in middle mantle, however, remains challenging, as any seismic waves sampling the middle mantle will unavoidably propagate through and therefore are affected by the very heterogeneous upper mantle.

[3] The most enigmatic strong anomalies in the middle mantle observed so far are the seismic reflectors and/or scatterers [*Fukao et al.*, 1988; *Kawakatsu and Niu*, 1994; *Niu and Kawakatsu*, 1997; *Kaneshima and Helffrich*, 1998;
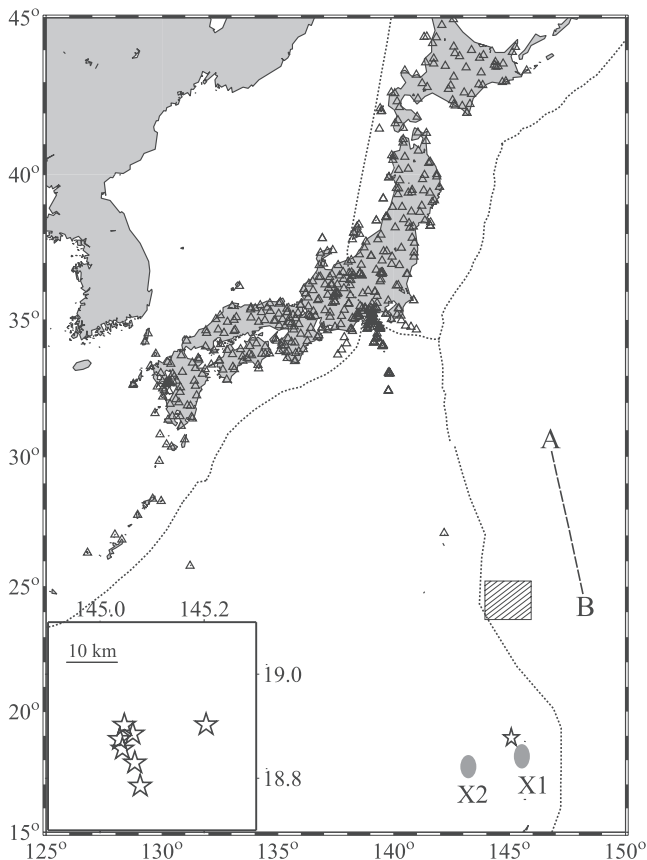
Figure 1. Map view of the locations of the seismic network and the cluster of Mariana deep earthquakes. The present-day plate boundary is indicated by dotted line. Dashed line AB shows the southward dipping lower-velocity layer at mid-lower mantle observed by *Kaneshima and Helffrich* [1999]. Shadowed ellipsoids labeled by X1 and X2 represent the locations of the two scatterers at the top of the lower mantle reported by *Kruger et al.* (2001). The shaded region marks the location of a midmantle reflector detected by this study. Star indicates the location of the deep Mariana cluster. Inset shows epicenters of the eight earthquakes used in this study. Seven of them occurred in 1995 with source depths of ~600 km, and one occurred in 1993 with a depth ~500 km. Locations are from *Kaneshima and Helffrich* [1998].

Vinnik et al., 1998; *Kaneshima and Helffrich*, 1999; *Castle and Creager*, 1999; *Vinnik et al.*, 2001; *Kruger et al.*, 2001]. Depths of these seismic reflectors/scatterers are reported to be at 800 km (uppermost lower mantle), 900–1200 km (midmantle) and down to ~1850 km (mid-lower mantle). Differences in S wave velocity between the reflectors/scatterers and the surrounding mantle could be as high as 4%. As all these reflectors/scatterers have been observed in the western Pacific subduction regions, these structures have been suggested to be related to the subducted slabs [*Niu and Kawakatsu*, 1997; *Kaneshima and Helffrich*, 1998, 1999; *Castle and Creager*, 1999; *Kruger et al.*, 2001]. *Kaneshima and Helffrich* [1999] speculated that the strong seismic scatterers in mid-lower mantle east of the Mariana and Izu-Bonin subduction zones might represent ancient oceanic crust. However, current knowledge on the shear modulus of the mineral assemblages of basalt at mid-lower mantle conditions is still not enough to provide robust inference. Moreover, slab associated high-velocity anomalies (hereafter referred to as HVAs) are not observed by global tomographic models [*van der Hilst et al.*, 1997; *Grand et al.*, 1997; *Fukao et al.*, 2001] around the mid-lower mantle scatterers. The interpretation of the seismic reflectors/scatterers is therefore still unknown, nor the physical mechanisms capable of producing these seismic structures.

[4] A sequence of middle-sized deep earthquakes occurred at northern Mariana subduction zone in the August of 1995 (Figure 1 and Table 1). High-quality relocation analyses [*Wiens et al.*, 1996; *Engdahl et al.*, 1998; *Kaneshima and Helffrich*, 1998; *Kruger et al.*, 2001] suggest that these earthquakes are separated from each other by only few to tens of kilometers, and therefore might be categorized as tightly clustered events. These earthquakes are the first good sized deep events that occurred in this region since the beginning of worldwide digital seismic recording. High-quality waveform data are recorded by both regional and global seismic networks. These seismograms show very interesting features and have revealed many significant structures in the deep interior of the earth. *Kaneshima and Helffrich* [1998, 1999] found several later arrivals after P from recordings of several short-period networks in the west coast of the United States. They measured the slowness, arrival time and back azimuth of the two particular arrivals ~90 and 105 s after P, and found that the arrivals are scattered energies by seismic scatterers at depths around 1600 and 1850 km east of the Mariana and Izu-Bonin subduction (AB, Figure 1). Meanwhile, *Kruger et al.* [2001] examined the data of Warramunga array in Australia from the same earthquakes and found two non-standard arrivals at 20.5 and 24 s after *P*. They interpreted these two arrivals as the *S-to-P* converted phases generated at reflectors/scatterers at depths of 790 and 720 km west of the cluster (X1 and X2, Figure 1). Here we report another later arrival shown in the seismograms of the same cluster recorded by a short-period seismic network in Japan. In this study, we will first constrain the geometrical and seismic properties of the seismic structure that generates the later arrival. We then discuss possible interpretations for the seismic structure, as well as their implications.

2. Seismic Observations

2.1. Source-Receiver Geometry

[5] The Mariana cluster of deep events is ~19° away from the Japanese islands (Figure 1). We use a short-period seismic network developed under Japan's national program for earthquake prediction. With an aperture size of 3000 km

Table 1. Event List

Event ID[a]	Latitude, °N	Longitude, °E	Depth, km	M_b
04/02/93_14:32	18.425	145.280	484.0	5.2
08/23/95_07:06	18.903	145.204	577.9	6.3
08/24/95_01:55	18.902	145.047	588.0	6.0
08/24/95_06:28	18.856	145.043	596.3	5.7
08/24/95_07:54	18.875	145.038	593.8	5.5
08/24/95_07:55	18.885	145.063	593.0	5.5
08/25/95_11:29	18.785	145.077	602.4	5.3
11/14/95_15:14	18.830	145.067	605.1	5.3

[a]Read 04/02/93_14:32 follows: 2 April 1993, 1432 UT.
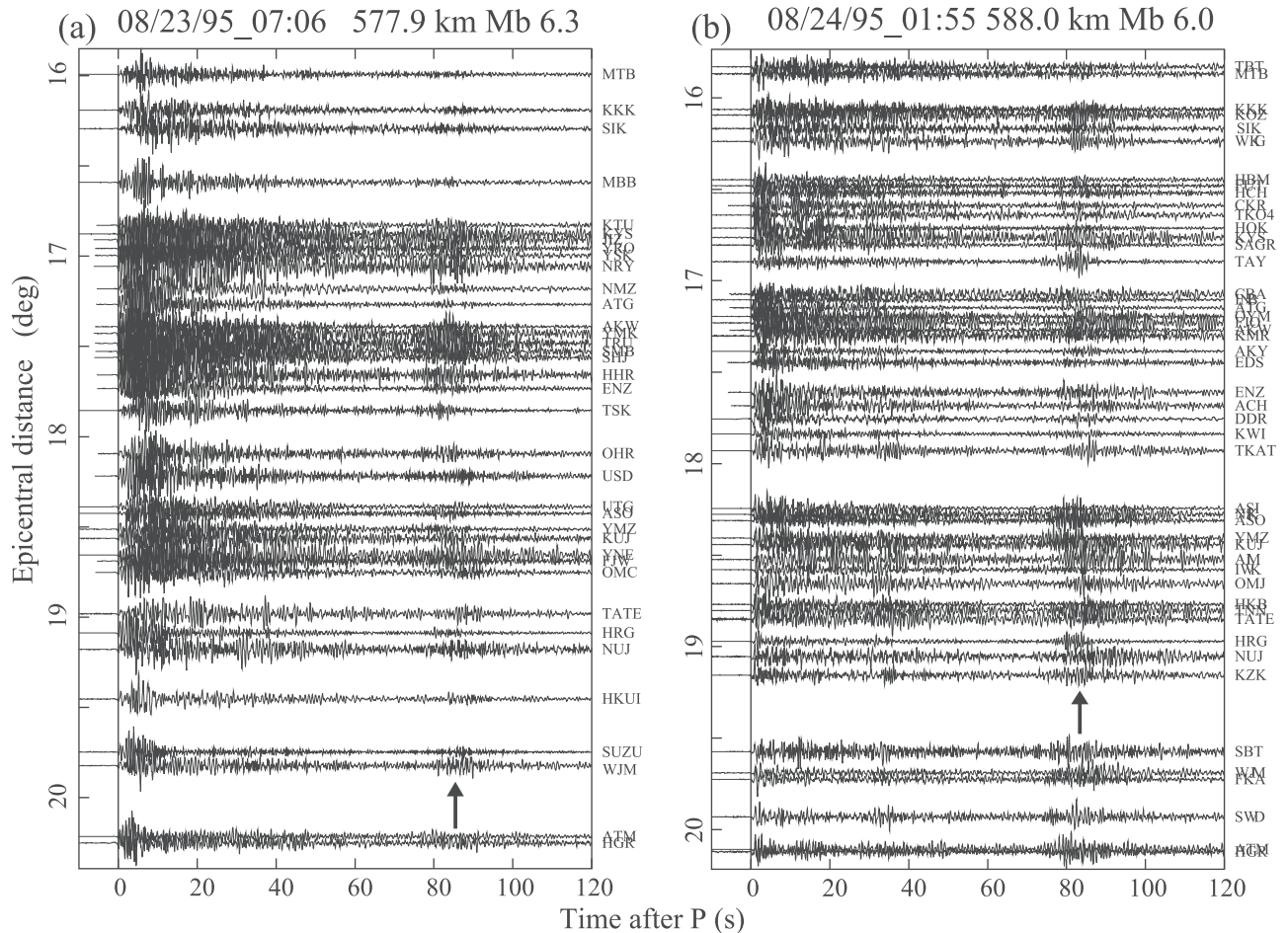
Figure 2. Two record sections of the J-array waveforms plotted in the order of epicentral distance for (a) event 08/24/95_01:55 and (b) event 08/23/95_07:06. Only a portion of J-array seismograms are shown for a clear display of waveforms. Waveforms are band-pass-filtered between 0.4 and 4 Hz and aligned along the arrival time of *P*, which is shifted to zero. The *x* phase is indicated by an arrow.

in length and 300–500 km in width, the network covers entire islands of Japan. The J-shaped seismometer array is usually referred as to J-array [*J-Array Group*, 1993] (Figure 1).

2.2. Observations of the Later Arrival

[6] We begin our presentation by showing J-array record sections of two deep earthquakes (Figure 2). Here we show only a portion of the J-array recording simply for the purpose of a clear display. All the seismograms are band-pass-filtered between 0.4 and 4 Hz and aligned at *P* arrivals, which is shifted to zero. Both record sections show clearly arrivals at ~80 s following *P* (hereafter referred as to *x* phase). While a later arrival could simply be the direct *P* wave of a closely followed aftershock, there are at least three facts that against this aftershock explanation, however. First of all, the aftershock explanation predicts a similar relative arrival time of the aftershock phases with respect to *P* among all the regional arrays. As mentioned in the introduction, the reported arrival times of the later phases vary from network to network [*Kaneshima and Helffrich*, 1998, 1999; *Kruger et al.*, 2001]. Second, it is very hard to explain the observation that the later arrivals show up on all the earthquakes just by coincidence. Finally, an aftershock phase will have the same slowness of P at teleseismic

distances, while the arrival times of the 80 s phase show a small decrease with distance (Figure 2).

[7] Theoretically, the *x* phase could be generated by a seismic anomaly near the source, receiver or somewhere between them. In the following subsections, we will determine the wave type (*P* or *S*) of the *x* phase and measure its slowness (incident angle), arrival time and arrival azimuth (back azimuth) in order to nail down its origin.

2.3. Features of the *x* Phase

[8] The *x* phase is also visible on vertical components of several broadband seismograms (Figure 3a). The particle motion of the *x* phase clearly shows a *P* wave feature (Figure 3b), suggesting that it is either an *S*-to-*P* converted phase or *P*-to-*P* reflected phase.

[9] The arrival times of the *x* phase at a single station show no significant difference among the 1995 earthquakes (Figure 4a). We notice that all the 1995 earthquakes occurred at more or less the same depth (Table 1). The *x* phase, however, arrives ~10 s later from the 1993 earthquake which is ~100 km shallower than the 1995 events (Figure 4b). This feature indicates that *x* phase is a downgoing wave when it takes off from the source.

[10] We used the beam-forming or slowness-azimuth stacking technique [*Aki and Richards*, 1980; *Niu and*
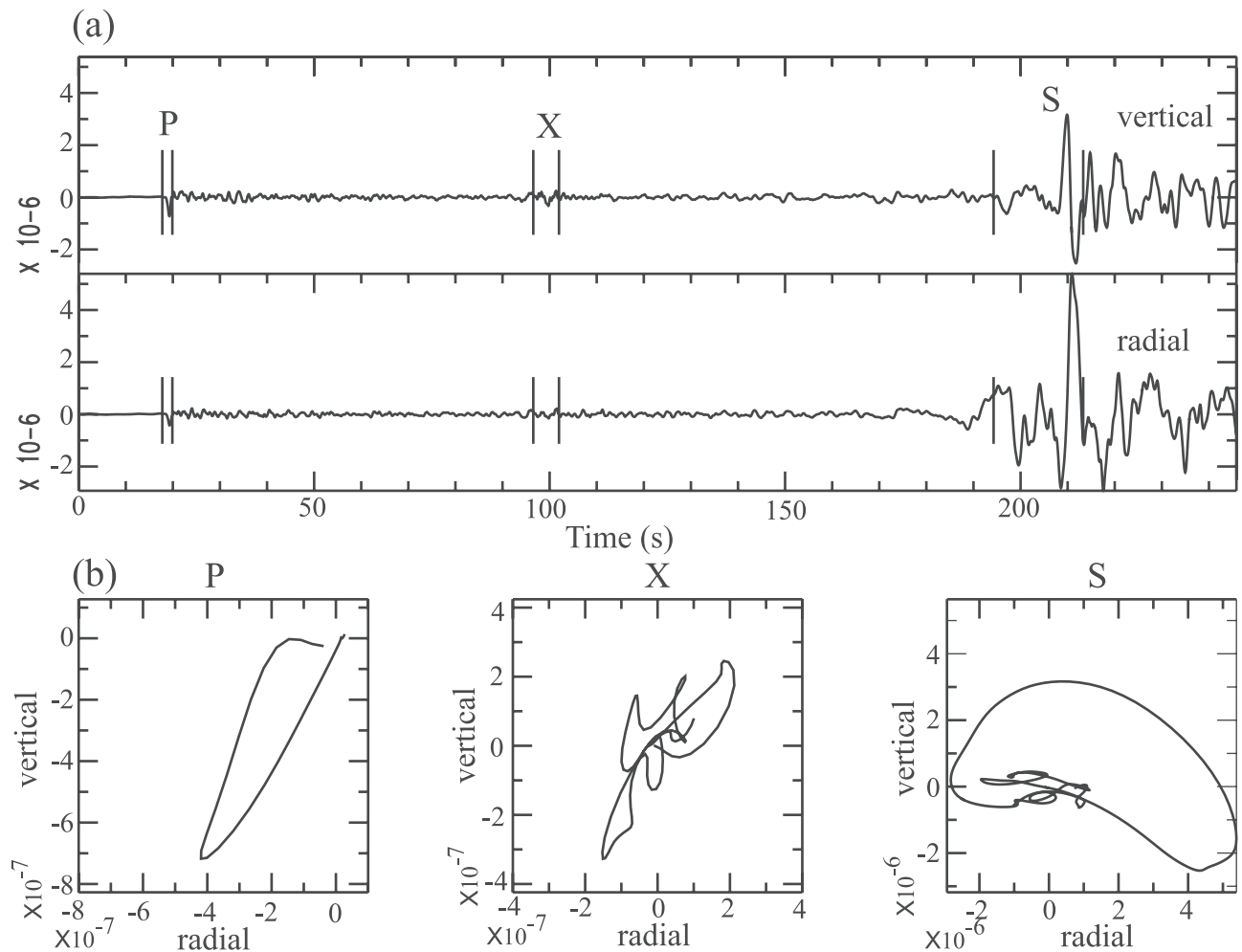
Figure 3.   (a) Broadband displacement waveforms of vertical and radial components at station HRG of event 08/24/95_01:55. (b) Particle motions of the *P*, *x*, and S waves. The *x* phase shows a similar particle motion as *P*.

Kawakatsu, 1997; *Kaneshima and Helffrich*, 1998] to measure the slowness and back azimuth of the *x* phase. In a beam-forming analysis, all the seismograms are *n*th root stacked [*Muirhead*, 1968] after a time correction calculated from the assumed slowness and back azimuth before stacking. The best slowness and back azimuth were determined when the *n*th root stacking amplitude reaches to a maximum (Figure 5). We varied slowness from 5 to 12 s deg^{-1} at increments of 0.1 s deg^{-1}, and searched the back azimuth deviation from the great circle path within a range of ±20° at increments of 2°. The measured slowness is ~1.9 s deg^{-1} smaller than that of *P*, indicating a steeper incident angle of the *x* phase. This observation is consistent with the interpretation of the *x* phase as a downgoing wave. The back azimuth of the *x* phase shows a slight deviation (~5°) from the great circle ray path, suggesting the related seismic anomaly is not located along the great circle path.

2.4. Phase Identification

[11]   To summarize, the *x* phase has the following features: (1) shows a *P* wave particle motion; (2) arrives later from earthquakes with shallower focal depth; (3) has a steeper incident angle than that of *P* wave; and (4) shows a deviation of a few degree in the arrival azimuth of the

great circle ray path. In addition, there is no other nonstandard phase identified from the array recordings at various time windows. On the basis of these features, we inferred that it is either an *S*-to-*P* or a *P*-to-*P* reflected or scattered wave generated by a seismic anomaly located below the source (Figure 6). We further argue that the seismic anomaly can not be an isotropic scatterer; otherwise, *S*-to-*S* scattered wave should have been also observed. The seismic anomaly appears more likely to be a reflector, as it scatters energy only to certain direction. It also can be shown from three-dimensional ray tracing that the *x* phase is unlikely to be a *P*-to-*P* reflected wave associated with a deeper reflector (Figure 6); as such a wave can not explain the observed arrival time and slowness simultaneously. Accordingly, the only plausible interpretation for the *x* phase is an *S*-to-*P* conversion wave reflected at a dipping reflector (Figure 6). In the following sections, we will use *SP* instead of *x* to refer the *x* phase.

3.   Mapping the Seismic Reflector
3.1.   Three-Dimensional Ray Tracing

[12]   We developed a three-dimensional ray tracing code for the purpose of determining the three-dimensional ge-
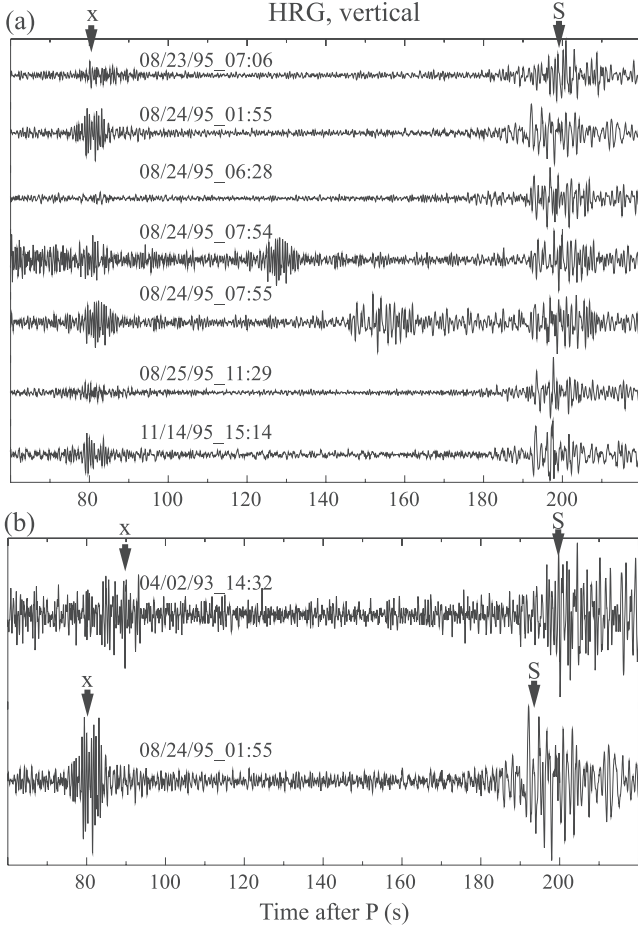
Figure 4. (a) Seismograms observed at station HRG for the seven events that occurred in 1995. They are aligned with the *P* arrivals and normalized by the maximum amplitude of *S* waves. No significant difference is observed in the arrival time of the *x* phase. (b) Two seismograms of events 04/02/93_14:32 and 08/24/95_01:55. They are plotted in the same manner of Figure 4a. The *x* phase arrives ~10 s later for the shallower event 04/02/93_14:32 compared to event 08/24/95_01:55.

ometry of a seismic reflector. Starting from a point in the reflector, we first use one-dimensional ray tracing to find the two ray paths that join the start point to the source and receiver, respectively. We represent the incident and reflected directions as two three-dimensional unit vectors **n₁** and **n₂** (Figure 7). On the basis of Snell's law, the normal vector of the reflector of the *S*-to-*P* reflection, **n** is

$$\mathbf{n} = l_2\mathbf{n_2} + l_1\mathbf{n_1}, \tag{1}$$

where l_1 and l_2 are

$$l_1 = \left(1 + \frac{v_s^2}{v_p^2} + 2(\mathbf{n_1} \cdot \mathbf{n_2})\frac{v_s}{v_p}\right)^{-\frac{1}{2}}$$
$$l_2 = \left(1 + \frac{v_p^2}{v_s^2} + 2(\mathbf{n_1} \cdot \mathbf{n_2})\frac{v_p}{v_s}\right)^{-\frac{1}{2}}. \tag{2}$$

We then search for the point at the reflector whose **n** calculated from (1) coincides with the normal vector of the reflector plane.

3.2. Travel Time Inversion

[13] Following the methods used in determining the Conrad discontinuity and upper boundary of subducted Pacific slab beneath Japan [*Horiuchi et al.*, 1982; *Matsuzawa et al.*, 1986; *Ohmi and Hori*, 2001], we assume the reflector as a plane surface which is expressed by

$$d(x,y) = d_0 + d_1(x - x_0)c_1 + d_2(y - y_0)c_2, \tag{3}$$

where *d* is the depth of the reflector at a location of (*x*, *y*), and (*x₀*, *y₀*) is a reference location. The two horizontal axes *x* and *y* are the latitude and longitude (in degree), respectively, and c_1 and c_2 are two constants of unit conversion from degree to kilometer in the two directions.

[14] Our goal is to determine the three parameters, d_0, d_1, and d_2 of the seismic reflector using the observed arrival times of the transmitted/reflected phase, t_{sp}^o. We apply an iterative approach to match the calculated time of the *S*-to-*P* wave at the reflector, t_{sp}^c to the observations, t_{sp}^o. The arrival time of the *S*-to-*P* reflection wave, t_{sp}^c, is a function of reflection depth *d*, and therefore a function of the three parameters, d_i,

$$t_{sp}^c = t_{sp}^c(d) = t_{sp}^c(d_0, d_1, d_2). \tag{4}$$

Using Taylor's expansion, we write t_{sp}^c as

$$t_{sp}^c(d_0, d_1, d_2) = t_{sp}^c(d_0^0, d_1^0, d_2^0) + \frac{\partial t_{sp}^c}{\partial d_0}\delta d_0 + \frac{\partial t_{sp}^c}{\partial d_1}\delta d_1 + \frac{\partial t_{sp}^c}{\partial d_2}\delta d_2, \tag{5}$$

where δd_i is a small variation from an initial value d_i^0. Using equation (3), we further rewrite the three first order partial derivatives as

$$\frac{\partial t_{sp}^c}{\partial d_0} = \frac{\partial t_{sp}^c}{\partial d}; \frac{\partial t_{sp}^c}{\partial d_1} = \frac{\partial t_{sp}^c}{\partial d}(x - x_0)c_1; \frac{\partial t_{sp}^c}{\partial d_2} = \frac{\partial t_{sp}^c}{\partial d}(y - y_0)c_2. \tag{6}$$

To obtain $\partial t_{sp}^c/\partial d$ in equation (6), we examined how the travel time of the *S*-to-*P* reflection phase is affected by a
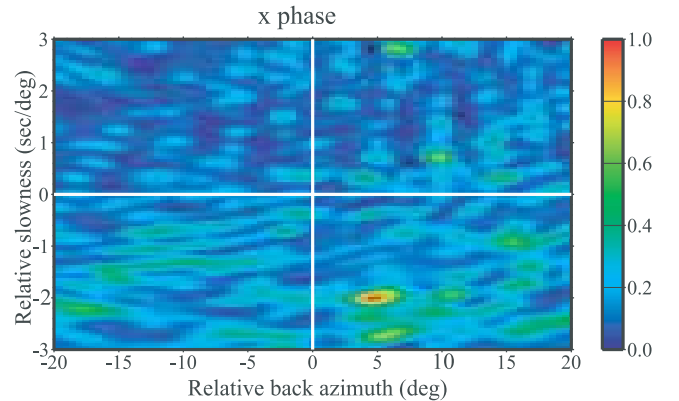
Figure 5. Normalized energy of the stacked *x* phase, shown as a function of back azimuth and slowness. Both back azimuth and slowness are relative to *P*. A time window of 4 s is used in calculating energy. The *x* phase reaches the maximum at a slowness of 1.9 s deg⁻¹ smaller than that of *P* and at a back azimuth of 5° deviated from the great circle ray path.

Station

P

Source

P

S

P   P
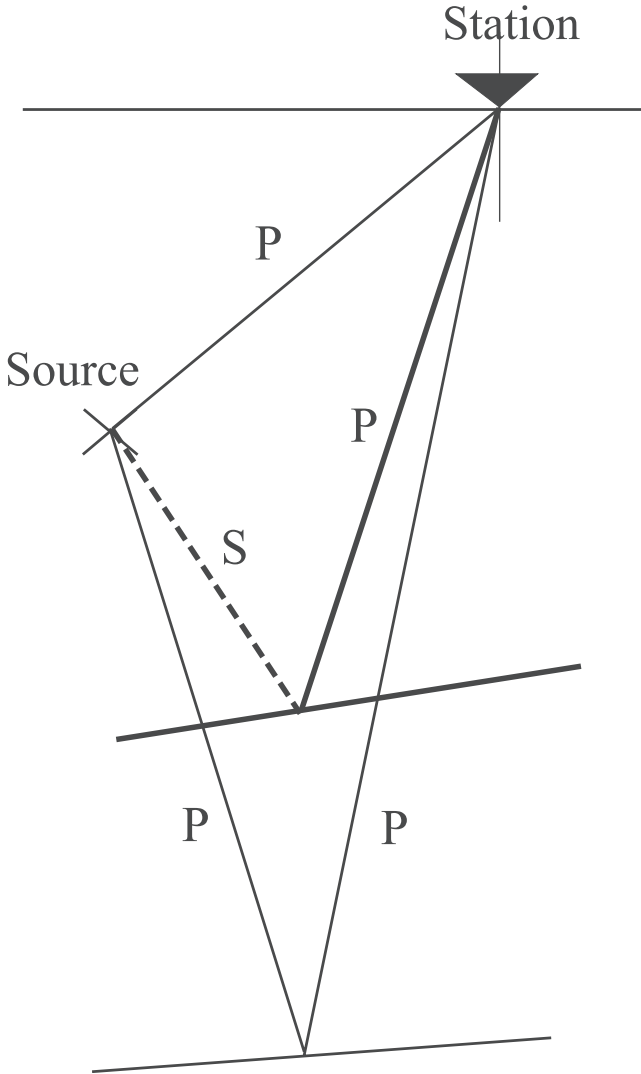
Figure 6. Schematic ray paths of S-to-P and P-to-P reflections at dipping reflectors.

small variation in the depth of the reflector. As shown in Figure 8, a small increase in the depth of the reflector, δd, results in an increase of the S and P wave ray paths by $\delta d \cos \beta$ and $\delta d \cos \alpha$, respectively. The total change in the travel time due to δd is

$$\frac{\partial t_{sp}^c}{\partial d} = \frac{\cos \beta}{v_s} + \frac{\cos \alpha}{v_p}, \tag{7}$$

where β and α are the incident and reflected angles, respectively (Figure 8). Therefore we have

$$\frac{\partial t_{sp}^c}{\partial d} = \frac{\cos \beta}{v_s} + \frac{\cos \alpha}{v_p}. \tag{8}$$

Using equations (6) and (8), the calculated travel time of the S-to-P reflection from the reflector can be written as

$$t_{sp,i}^c = t_{sp,i}^{c,0} + \left(\frac{\cos \beta}{v_s} + \frac{\cos \alpha}{v_p} \right) \delta d_0 + c_1 (x_i - x_0) \left(\frac{\cos \beta}{v_s} + \frac{\cos \alpha}{v_p} \right)$$

$$\cdot \delta d_1 + c_2 (y_i - y_0) \left(\frac{\cos \beta}{v_s} + \frac{\cos \alpha}{v_p} \right) \delta d_2 \tag{9}$$

at a single station, i, and

$$\mathbf{t} = \mathbf{t}^0 + \mathbf{A}\mathbf{x} \tag{10}$$

or a total of N stations. Here $\mathbf{A}$ is a $N \times 3$ matrix, and $\mathbf{x} = (\delta d_0, \delta d_1, \delta d_2)^T$. We employed a least squares approach to minimize the misfit between t_{sp}^c and t_{sp}^o, which leads to a solution of $\mathbf{x}$ as

$$\mathbf{x} = \left(\mathbf{A}^T \mathbf{A} \right)^{-1} \mathbf{A}^T (\mathbf{t}^o - \mathbf{t}^{c,o}). \tag{11}$$

Once we obtain δd_i, we replace d_i by $d_i + \delta d_i$. We then retrace ray paths of the S-to-P reflection waves using the new reflector geometry and repeat the above inversion process. The iteration continues until the misfit of the S-to-P travel time reaches stable.

3.3. Geometrical Properties of the Seismic Reflector

[15] We handpicked a total of 427 arrival times of the SP phase from more than one thousand J-array seismograms. As shown in Figure 3, it is very difficult and almost impossible to read the onset of the SP phase from short-period seismograms (upper, Figures 9a and 9b). We tried to take the cross correlation between the SP phase and the direct P wave to pick the SP, the complicated waveform of P due to the triplication, however, results in a very low value of correlation (middle, Figures 9a and 9b). It is therefore also difficult to pick the arrival time of the x phase by the conventional cross-correlation method. In this study, we used a simple running average method. We first calculate the running average of absolute amplitude from each individual seismogram. We then pick the maximum amplitude of both P and SP phases in the running average. As shown in Figure 9, it is relatively easy to pick the SP phase in the running averages, even if the amplitude of the SP phase is not so large (Figure 9b). Because of the uncertainty

Z

Y

$\mathbf{n}$ $\mathbf{n_2}$

l_1 P

$\mathbf{n_1}$

l_2

S

X
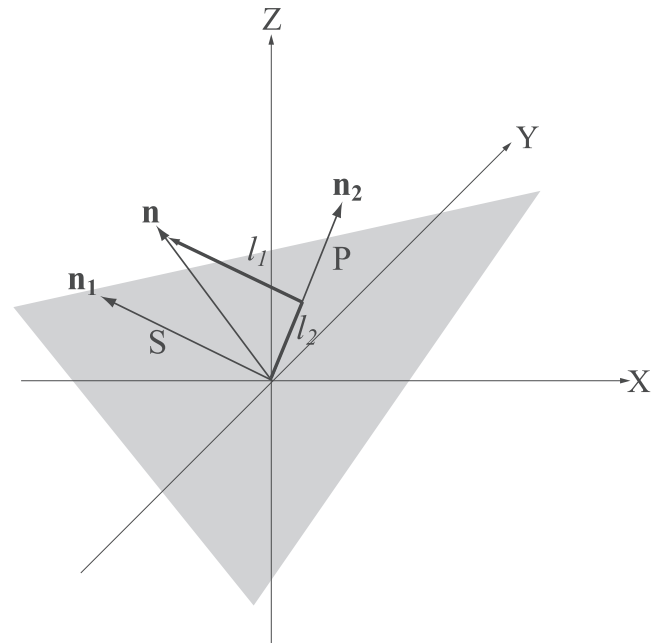
Figure 7. Three-dimensional ray geometry of S-to-P reflection. $\mathbf{n_1}$, $\mathbf{n_2}$ and $\mathbf{n}$ are the incident, reflected and normal vectors, respectively.
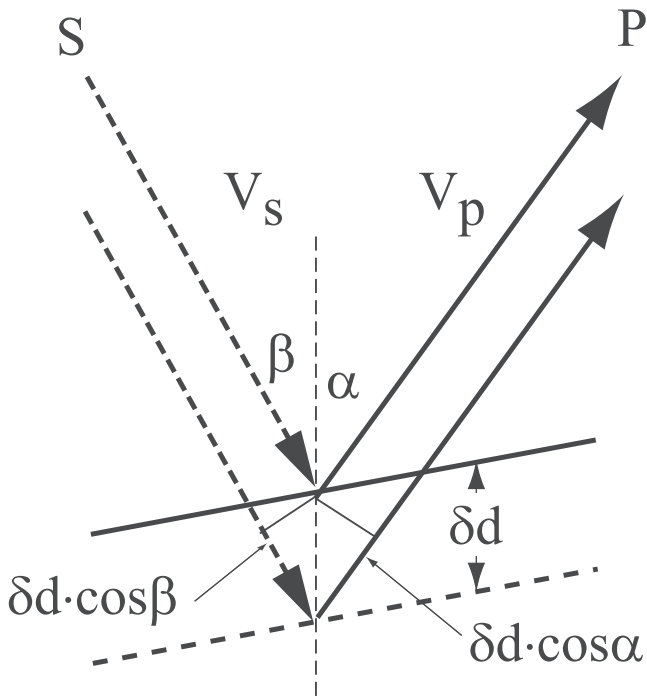
Figure 8. Cartoon showing change in S-to-P reflection travel time due to a subtle increase of the depth of the reflector.

in pickings of P and SP, we expect an error of less than 2 s in the SP-P differential travel time data, t_{sp}^o. A 2 s error of time pick will result in an uncertainty $\sim$10 km in depths of the reflector.

[16] We started from a horizontal reflector at 1140 km, and a reference location of (24.0°N, 144.0°E). After 12 iterations, the resulted (d_0, d_1, d_2) are (1140 km, −0.3403, −0.1595), which corresponds to a normal vector of 108.6°, 98.6°, 20.4° from north, east, and vertical directions, respectively. The average travel time residual reduction is reduced from $\sim$3.5 to 1.6 s. About 86% of the observed SP-P differential time, t_{sp}^o, is fitted within the error range. The S-to-P reflection points are plotted in Figure 10. The reflector dips southwest by $\sim$20°, with a lateral extension at least 100 by 100 km.

3.4. Seismic Properties of the Seismic Reflector

[17] There are several interesting features shown in the observed amplitude of the SP phase. It might have been already noticed from Figure 5 that there is a large variation in the observed amplitude of the SP phase from different earthquakes recorded by a same station. Since all the earthquakes are tightly clustered, the paths which seismic waves (i.e., P, S, and SP) propagate from these earthquakes to a station are almost same; such a variation is not expected to be resulted from heterogeneities along the ray paths. Instead, the amplitude variation must be directly related to a difference in the radiated energy from the sources due to different focal mechanism. In Figure 11, we show the observed relative amplitude ratio of the SP phase with respect to the S wave (A_{SP}/A_S) observed at station HRG as a function of the predicted ratio computed from the Harvard centroid moment tensor (CMT) solutions [*Dziewonski et al.*,

1981]. Both the calculated and observed ratios are normalized by the ratio of the reference event 08/24/95_01:15, which has the largest amplitude ratio of A_{SP}/A_S. It is clear from Figure 11 that the observed large variations in the amplitude of the SP phase can be explained very well by source mechanism. The good agreement between the observed and predicted amplitude ratio of A_{SP}/A_S, on the other hand, increases our confidence in the interpretation of the x phase as an S-to-P reflection. Here, we also want to emphasize the importance of the slight deviation from the great circle ray path of SP phase in explaining the amplitude data. Without this deviation in radiation azimuth, the predicted ratio of A_{SP}/A_S will not match the observation as well as that shown in Figure 11.
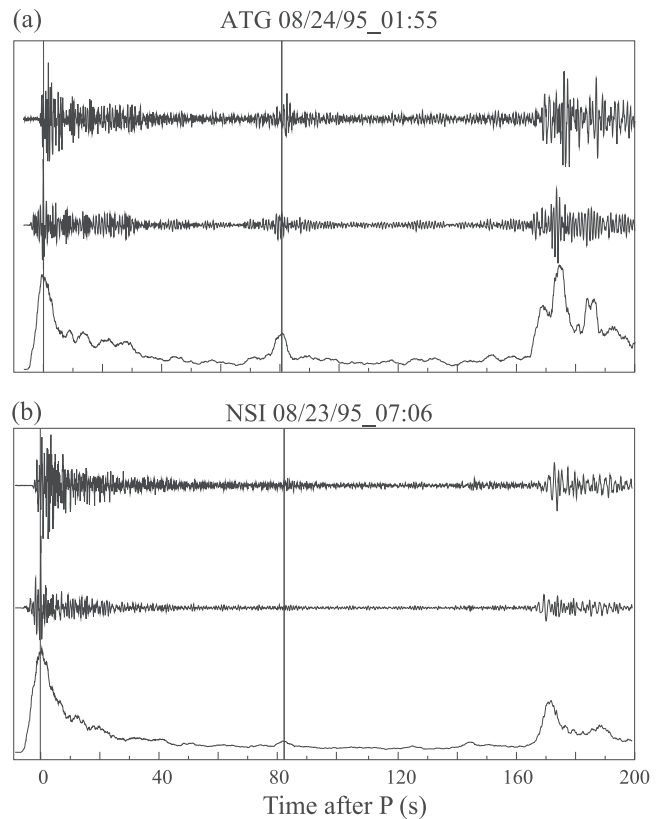
Figure 9. (a) Two examples of original seismograms (top), their running cross correlations with the direct P waves (middle) and running averages of the absolute amplitude (bottom). A time window of 4 s, which is comparable with the source duration, is used in the calculation of cross correlation and running average. Reading the onset of the x phase is almost impossible (top). It is also difficult to pick the arrival time of the x phase by taking the cross correlation between the x phase and the direct P wave due to the complicated waveforms of P and high frequency (middle). (b) The x phase is, however, relatively easy to pick in the running averages, even if the amplitude of the x phase is not so large. Also as shown in Figure 9a, there is slightly difference (1.2 s) in the picking times in the running average and cross-correlation methods. We therefore estimate an error of ≤2s in the SP-P differential travel time data, t_{sp}^o, by picking the maximum of the running average.
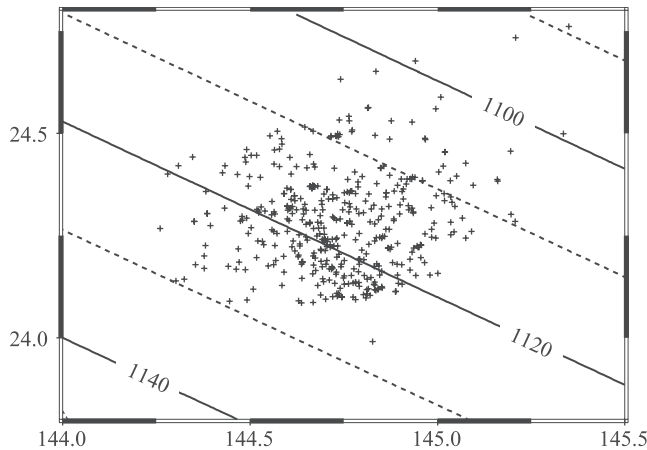
Figure 10. Contour map that shows the depths of the upper boundary of the reflector. *S*-to-*P* reflection points are denoted by crosses.

[18] Among the eight earthquakes used here, we are able to find the source mechanism solutions of the two largest events from the U.S. Geological Survey (USGS) catalog [*Sipkin and Zirbes*, 1997]. The USGS mechanisms are very similar to the Harvard solutions. The *T*, *P*, and *N* axes from the two catalogs are separated less than 3°. As a result, the calculated A_{SP}/A_S of event 08/23/95_07:06 from the USGS mechanism, which is shown as the open circle in Figure 11, is only slightly different from the CMT prediction.

3.4.1. Velocity and Density Structure Within the Reflector

[19] We also found that the amplitude ratio (A_{SP}/A_S) from a similar earthquake varies significantly among different stations. A_{SP}/A_S observed from all the 8 events consistently shows an increase with the incident angle of the *SP* phase (Figure 12a). A rapid increase in A_{SP}/A_S is observed from all the earthquakes just before the critical angle of *S*-to-*P* reflection (~33.7°). The incident angle is calculated from the three-dimensional ray geometry shown in Figure 10. We used the iasp91 model [*Kennett and Engdahl*, 1991] in the ray tracing. We averaged the *SP-P* differential travel time data, t_{sp}^o, at a binning angle interval of 0.1°.

[20] The observed features of A_{SP}/A_S and the negative polarity of the *SP* phase shown in broadband seismograms (Figure 3a) place tight constraints on the possible velocity and density models within the reflector. While the amplitude ratio is a complicated function of combined *P*, *S* wave velocity and density contrasts between the mantle and the reflector, the critical angle is determined by the Poisson's ratio in the mantle above the reflector. The observed critical angle in Figure 12a shows a good agreement with the prediction of the iasp91 model. Therefore we used the iasp91 as the mantle model and adjusted the velocity and density models within the reflector to fit the observations.

[21] The amplitude ratio A_{SP}/A_S can be expressed as products of several different effects:

$$\frac{A_{SP}}{A_S} = \left(\frac{A_{SP}}{A_S}\right)_S \left(\frac{A_{SP}}{A_S}\right)_Q \left(\frac{A_{SP}}{A_S}\right)_G \left(\frac{A_{SP}}{A_S}\right)_R \left(\frac{A_{SP}}{A_S}\right)_r, \qquad (12)$$

where subscripts *S*, *Q*, *G*, *R*, and *r* represent effects due to the source, attenuation, geometrical spreading, receiver

response and *S*-to-*P* reflection coefficient, respectively. We used the Harvard CMT solutions in calculating $(A_{SP}/A_S)_S$. We computed respectively $(A_{SP}/A_S)_G$ and $(A_{SP}/A_s)_R$ by using the length of the ray paths and the incident angles of the *S* and *S*-to-*P* reflection waves. A $\delta t^*_{SP-S} = -0.7$ based on the PREM *Q* model [*Dziewonski and Anderson*, 1981] is assumed in calculating $(A_{SP}/A_S)_Q$. Since the ray paths of *S* waves and *S*-to-*P* reflection waves are very different from each other (Figure 6), such an assumption could introduce large errors if the attenuation structure along the *S* and *S*-to-*P* reflection ray paths differs significantly from PREM.

[22] We have conducted an extensive search in both the velocity and density model spaces, as well as the transition thickness between the reflector and its surroundings. First, in order to explain the high amplitude observed at high-frequency (~1 Hz) seismograms a very sharp mantle reflector transition (≤2 km) is required in the reasonable velocity and density model spaces.

[23] Second, only models with a reduction (≥2%) in *S* wave velocity and almost no changes in *P* wave velocity (≤1%) within the reflector are found to be capable to explain the large amplitude (Figure 12a) and negative polarity (Figure 3a) of the *SP* phase. Third, the observed
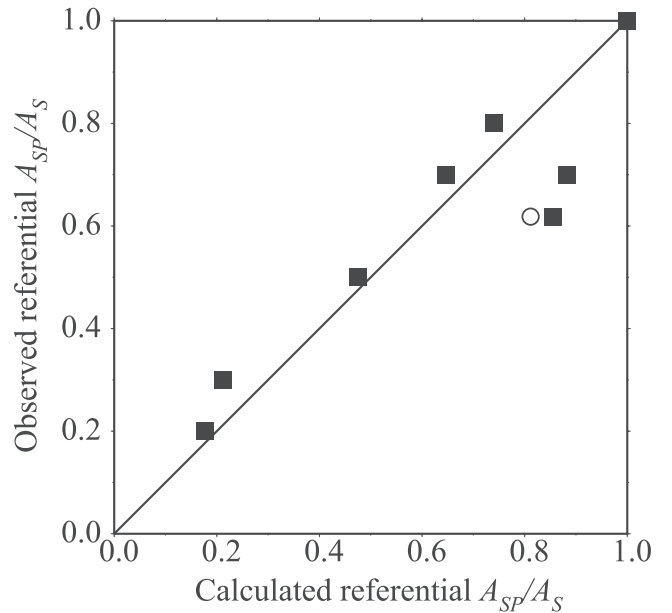
Figure 11. Relative amplitude ratio of the *SP* phase with respect to the *S* wave (A_{SP}/A_S) observed at station HRG as a function of the predicted ratio. Both the calculated and observed ratios are normalized by the ratio of the reference event 08/24/95_01:15, which has the largest A_{SP}/A_S ratio. Since all the earthquakes occurred at almost the same location, the ray paths of a particular seismic wave from these earthquakes to a station are nearly same. The referential ratio therefore depends only on the focal mechanisms of the earthquakes. The observed referential ratios show a good agreement with the predicted ones computed from Harvard CMT solutions. The calculated A_{SP}/A_S of event 08/23/95_07:06 from the USGS catalog is shown by the open circle, which is slightly left shifted from the CMT prediction.
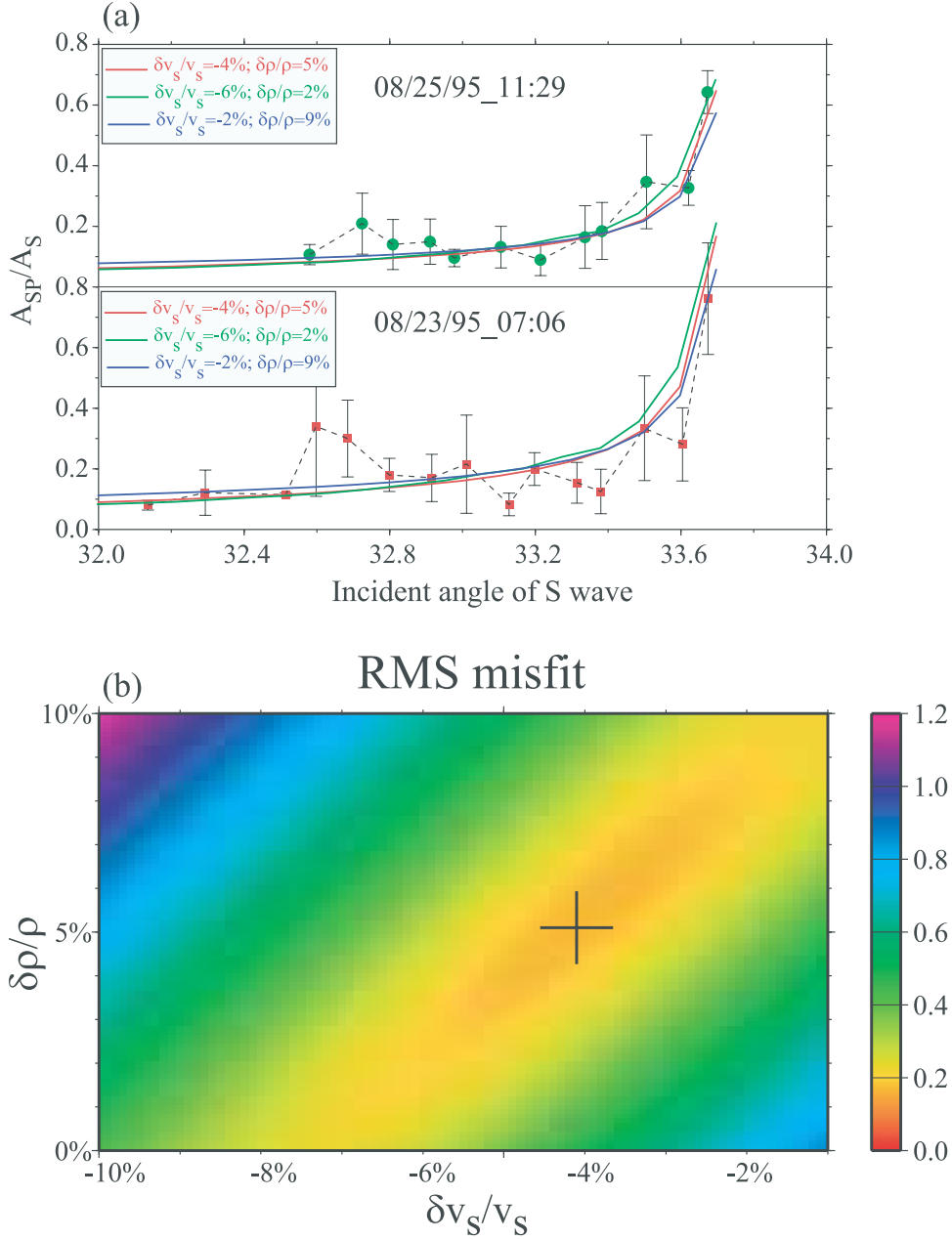
Figure 12. (a) Two examples that show the averaged A_{SP}/A_S ratio observed from events 08/25/95_11:29 (solid circles) and 08/23/95_07:06 (solid squares). The incident angle is calculated from the three-dimensional ray geometry shown in Figure 10, and the SP-P differential travel time data, t_{sp}^o, is averaged at an interval of 0.1°. The observed A_{SP}/A_S shows a rapid increase just before the critical angle of S-to-P reflection. Also shown is the predicted A_{SP}/A_S from three models. (b) Averaged RMS misfits are shown as a function of S wave velocity and density changes within the reflector. Black cross indicates the model with the minimum RMS misfit.

A_{SP}/A_S curve favors models with an increase of density by several percent within the reflector.

[24] We applied a grid search to find the minimum of root-mean-square (RMS) misfits between the calculated and observed amplitude ratio, which is defined by

$$\left\{ \sum_{i=1}^{N} \frac{\left(\left. \frac{A_{SP}}{A_S} \right|_{ci} - \left. \frac{A_{SP}}{A_S} \right|_{oi} \right)^2}{\sigma_{oi}^2} \middle/ \sum_{i=1}^{N} \frac{\left(\left. \frac{A_{SP}}{A_S} \right|_{oi} \right)^2}{\sigma_{oi}^2} \right\}^{\frac{1}{2}} . \qquad (13)$$

Here, $(A_{SP}/A_S)_{ci}$, $(A_{SP}/A_S)_{oi}$, and σ_{oi} are the calculated, observed amplitude ratios and their standard deviations. In Figure 12b we show the RMS misfit as a function of S wave velocity and density contrasts between the surrounding mantle and the reflector. The best fitting model is characterized by a decrease of 4% in S wave velocity and an increase of ~5% in density within the reflector (black cross in Figure 12b). The predicted A_{SP}/A_S from this model is shown by a red line in Figure 12a. Since there are uncertainties in the calculation of A_{SP}/A_S and large errors in
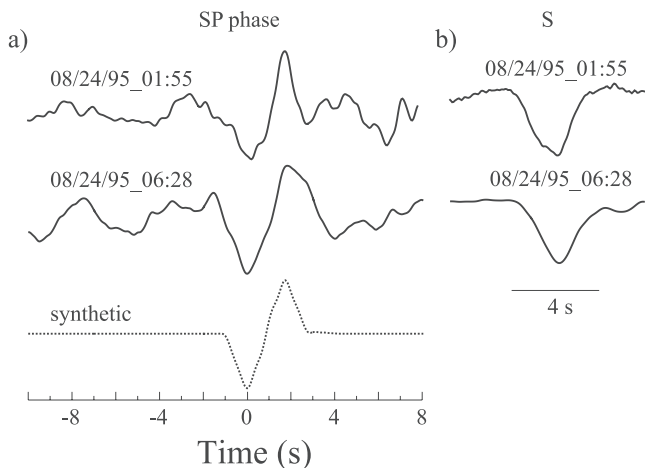
Figure 13. (a) Stacked displacement waveforms of the *SP* phase for events 08/24/95_01:55 and 08/24/95_06:28 are shown with a synthetic seismograms computed for a 12 km thick layer using Thomson-Haskell method [*Haskell*, 1962]. The *P*, *S* wave velocity and density within the layer are respectively 0%, −4%, and 5% higher than the surrounding mantle. (b) Stacked displacement waveforms of the *S* wave of events 08/24/95_01:55 and 08/24/95_06:28.

the observed A_{SP}/A_S, it is impossible and might be impropriate to resolve a single best model from the observations. In fact, we find that models with a reduction of 2–6% in *S* wave velocity and an increase of 2–9% in density can fit the observed data reasonably well within the error ranges (blue and green lines in Figure 12a).

3.4.2. Thickness of the Reflector

[25] We have 5–10 high signal-to-noise ratio broadband recordings for the two events, 08/24/95_01:55 and 08/24/95_06:28. We aligned these seismograms at the predicted time of the *S*-to-*P* reflection and applied a linear stacking technique [*Kanasewich*, 1973] to the aligned seismograms. The stacked displacement seismograms of the two events are shown in Figure 13a. Waveforms of the *SP* phase shown in Figure 13a consist of a negative pulse and a following positive one; while the direct *S* waves (Figure 13b) show a simple negative pulse. We interpret the second positive pulse of the *SP* phase as a second *S*-to-*P* reflection at the lower boundary of the reflector. The separation of the two pulses thus can be used to constrain the thickness of the reflector. By comparing the *SP* waveforms (Figure 13) with synthetic data, we estimated the thickness of the reflector to be ~12 km. Here we used Thomson-Haskell method [*Haskell*, 1962] and the iasp91 model in calculating the synthetic seismograms. While the estimated thickness here is sensitive to the V_p/V_s ratio of the reference model, we found the difference in V_p/V_s ratio at midmantle depth between different global models (FREM, iasp91, ak135 [*Kennett et al.*, 1995]) is very small (< 0.2%), and therefore our estimate is relatively model independent.

[26] There is a secondary peak at incident angle ~32.6° in the observed A_{SP}/A_S (Figure 12a), we interpret it to be caused by near critical *S*-to-*P* reflection at the lower boundary of the reflector. Since the v_s/v_p ratio within the reflector is lower than that of the surrounding mantle, the critical angle of *S*-to-*P* reflection at the lower boundary is

smaller than that at the upper boundary. If this interpretation is correct, then the relative location of the secondary to the primary peaks of A_{SP}/A_S in Figure 12a provides a tight constrain on the *S* wave velocity, a ~3% decrease, within the reflector. For such a velocity model, an increase of ~%7 in density is required to explain the large amplitude of A_{SP}/A_S (Figure 12b).

4. Discussion

[27] There are three observations of strong seismic reflectors at midmantle [*Niu and Kawakatsu*, 1997; this study] and mid-lower mantle depths [*Kaneshima and Helffrich*, 1998] so far. All the associated seismic phases can be identified from single seismograms. Each of these strong reflectors is observed at the western Pacific subduction zones. One was observed at the western end of the Indonesia arc; two are observed at the Izu-Bonin and Mariana
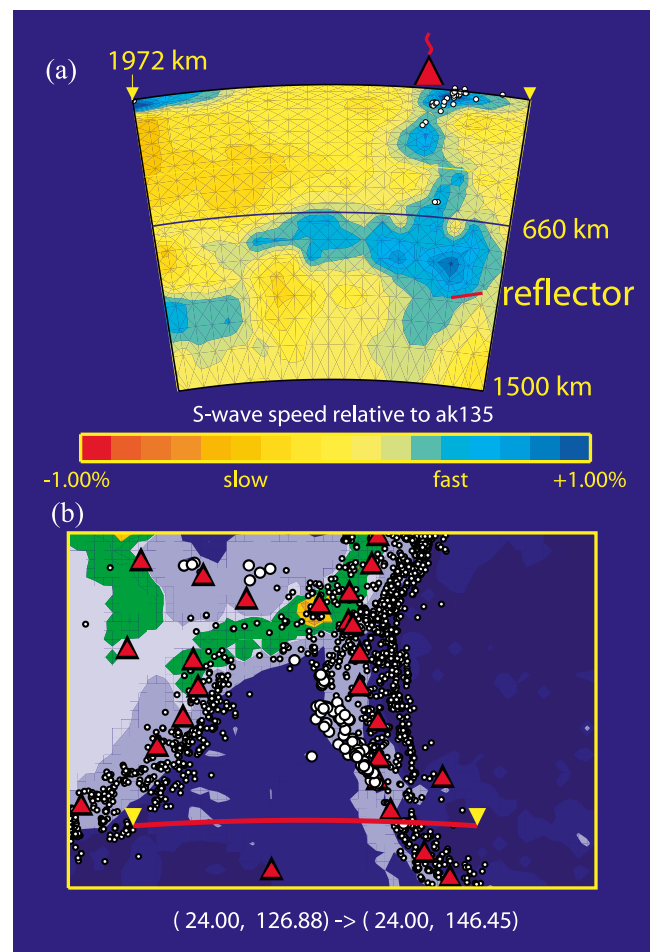
Figure 14. (a) A cross section showing the *S* wave velocity anomalies from a global tomographic model of *Widiyantoro et al.* [2000]. The strong seismic reflector observed by this study is plotted as a red line, which is located at the lower edge of a HVA. (b) Map shows the geographic location of the cross section of Figure 14a. Red triangles represent the volcanoes. Shallow and deep seismicity are indicated by small and large white circles, respectively.

subduction regions. The depths of the midmantle reflectors observed at the western end of the Indonesia are almost same, at ~1100 km. Both locate near the lower edge of a HVA in global tomographic models (Figure 14). On the other hand, there are no HVAs observed around the mid-lower mantle reflectors [*Kaneshima and Helffrich*, 1998].

[28] As these strong reflectors are detected only at the western Pacific subduction regions, it might be natural to associate these reflectors to subducted slabs. However, we want to emphasize that these seismic reflectors are actually very difficult to be detected from current seismic analyses unless a favored source-reflector-receiver geometry is provided. As shown the in the Figure 12a, if the incident angle is less than ~32°, the *S*-to-*P* reflection coefficient becomes so small that it is almost impossible to identified the *S*-to-*P* reflection from individual seismograms. On the other hand, beyond the critical angle, there will be no *S*-to-*P* reflection. Therefore it is still too early to conclude that such strong and sometimes dipping seismic reflectors are limited at the western Pacific subduction regions, although we noticed that several studies [*Vidale et al.*, 2001; *Castle and van der Hilst*, 2003] have been unsuccessful in finding these midmantle reflectors in other regions.

[29] Since the observed seismic reflector corresponds to a thin lower-velocity and high-density layer rather than an interface of velocity and/or density discontinuity, it is unlikely to be caused by a single phase transform of the lower mantle minerals. The large velocity and density contrasts and sharp transition between the reflector and its surrounding as well as the dipping feature suggested that the seismic reflector is more likely to be a chemical reservoir rather than a purely thermal anomaly. Two possible interpretations for such a chemical anomaly might be employed if the seismic reflector is related to subducted slabs.

[30] The observed seismic reflectors might be a piece of subducted oceanic crust, as suggested by *Kaneshima and Helffrich* [1999]. Recent experimental studies [*Hirose et al.*, 1999; *Ono et al.*, 2001] found that the mineral assemblages of basalt at ~1100 km depth are ~2% denser than the surrounding mantle. The observed density increase within the reflector is thus consistent with the oceanic crust explanation, although the experiment results lie at the lower bound of the observed 2–9% density increase. There is no in situ measurement of bulk and shear moduli of the mineral aggregation of basaltic composition at midmantle condition to date, it is still inconclusive whether the *P* and *S* wave velocities are higher (C. Bina, personal communication, 2002) or lower [*Kaneshima and Helffrich*, 1999] than those of the peridotite mantle at the same depth. Therefore this explanation still requires further confirmation from mineral physical data.

[31] On the other hand, if the oceanic crust interpretation of the midmantle and mid-lower mantle seismic reflectors could be finally confirmed, several interesting speculations might be made from our observations. The presence of the HVAs above the midmantle reflectors and the absence of HVAs around the mid-lower mantle reflectors may imply that the subducted oceanic crust starts sinking separately from the oceanic mantle lithosphere at depths greater than 1100 km. An alternative implication is that the seismic signatures of the oceanic mantle lithosphere might become indistinguishable from the surroundings at mid-lower mantle depths.

[32] An alternative scenario from our observations is possible "chemical/mechanical segregation" within subducted slabs at midmantle depths. Most of subducted slabs in the western Pacific tend to be deflected or flattened around the upper and lower mantle boundary [*Fukao et al.*, 2001]. Once they enter into the lower mantle, the distorted subducted slabs start to segregate chemically/mechanically into two parts. The evolved slabs consist of a major part with a lower density but a higher velocity and an underlying small part with a denser but lower seismic velocity. *Shieh et al.* [1998] reported that water may be brought down to the middle mantle by the subducting process in the form of dense hydrous magnesium silicates (DHMS). They found that in the cold and mature slabs the super hydrous phase D of DHMS can persist to ~1250 km and then breaks down into perovskite, periclase and possibly water. Such a break down of phase D may trigger the chemical segregation within slabs. After segregation the denser portion of the slabs which appears as strong seismic reflectors but is invisible from tomographic images keeps sink into the core mantle boundary.

5. Summary and Conclusions

[33] We have focused on analyzing and interpreting a clear later arrival ~80 s (*x* phase) after *P* that is observed in most of the individual recordings of a short-period seismometer network in Japan from a cluster of Mariana deep earthquakes. By combining the measured arrival slowness and azimuth of the *x* phase as well as the anticorrelation feature of its arrival time with focal depths, we concluded that the *x* phase is an *S*-to-*P* conversion wave reflected at a seismic reflector below the earthquakes. We developed a three-dimensional ray tracing scheme for the purpose of determining the orientation of the seismic reflector. We applied travel time inversion to the handpicked 427 arrival time to locate the seismic reflector that generates the *SP* phase. The seismic reflector is located at 24.25°N 144.75°E at depth ~1115 km and dips toward southwest by ~20°, with a lateral extension at least 100 by 100 km. A decrease of 2–6% in *S* wave velocity and an increase of 2–9% in density within the reflector are required in order to explain the large amplitude of the *SP* phase. One interpretation of the seismic reflector is that it is a piece of subducted oceanic crust, as suggested by a previous study [*Kaneshima and Helffrich*, 1999]. With this interpretation the absence of the HVAs around the strong scatterers at greater depths (~1600 and ~1850 km) in the global tomographic models might imply either that subducted oceanic crust starts to sink separately from the oceanic mantle lithosphere at depths greater than 1100 km or that the seismic signatures of the oceanic mantle lithosphere become indistinguishable from the surroundings at greater depths. We also speculate an alternative interpretation for the midmantle seismic reflector, which involves the break down of the *D* phase of dense hydrous magnesium silicates (DHMS) at the cold slab and midmantle pressure conditions reported by recent mineral physics studies [*Shieh et al.*, 1999; *Ohtani et al.*, 2001]. Both scenarios suggest either mechanical or chemical segregation may occur within subducted slabs once they enter into the lower mantle.

References

Aki, K., and P. G. Richards, *Quantitative Seismology: Theory and Methods*, 932 pp., W. H. Freeman, New York, 1980.

Castle, J. C., and K. C. Creager, A steeply dipping discontinuity in the lower mantle beneath Izu-Bonin, *J. Geophys. Res.*, *104*, 7279–7292, 1999.

Castle, J. C., and R. D. van der Hilst, Searching for seismic scattering off mantle interfaces between 800 km and 2000 km depth, *J. Geophys. Res.*, *108*(B2), 2095, doi:10.1029/2001JB000286, 2003.

Cleary, J. R., and R. A. Haddon, Seismic wave scattering near the core-mantle boundary: A new interpretation of precursors to *PKP*, *Nature*, *240*, 549–551, 1972.

Davaille, A., Simultaneous generation of hotspots and superswells by convection in a heterogeneous planetary mantle, *Nature*, *402*, 756–760, 1999.

Dziewonski, A. M., and D. L. Anderson, Preliminary reference Earth model, *Phys. Earth Planet. Inter.*, *25*, 297–356, 1981.

Dziewonski, A. M., T.-A. Chou, and J. H. Woodhouse, Determination of earthquake source parameters from waveform data for studies of global and regional seismicity, *J. Geophys. Res.*, *86*, 2825–2852, 1981.

Engdahl, E. R., R. D. van der Hilst, and R. P. Buland, Global teleseismic earthquake relocation with improved travel times and procedures for depth determination, *Bull. Seismol. Soc. Am.*, *88*, 722–743, 1998.

Fukao, Y., K. Kanjo, and S. Hori, Seismic reflector near the leading edge of the subducted slab (in Japanese), *Program Abstr. 2*, p. 82, Seismol Soc. of Jpn., Tokyo, 1988.

Fukao, Y., S. Widiyantoro, and M. Obayashi, Stagnant slabs in the upper and lower mantle transition zone, *Rev. Geophys.*, *39*, 291–323, 2001.

Garnero, E. J., and D. V. Helmberger, A very slow basal layer underlying large-scale low-velocity anomalies in the lower mantle beneath the Pacific: Evidence from core phases, *Phys. Earth Planet. Inter.*, *91*, 161–176, 1995.

Grand, S. P., R. D. van der Hilst, and S. Widiyantoro, Global seismic tomography: A snapshot of convection in the Earth, *GSA Today*, *7*, 1–7, 1997.

Haskell, N. A., Crustal reflections of the plane *P* and *SV* waves, *J. Geophys. Res.*, *67*, 4751–4767, 1962.

Hirose, K., Y. Fei, Y. Ma, and H. Mao, The fate of subducted basaltic crust in the Earth's lower mantle, *Nature*, *397*, 53–56, 1999.

Horiuchi, S., H. Ishii, and A. Takagi, Two-dimensional depth structure of the crust beneath the Tohoku district, the northeastern Japan arc: Part 1. Method and Conrad discontinuity, *J. Phys. Earth*, *30*, 47–69, 1982.

J-Array Group, The J-Array program: System and present status, *J. Geomagn. Geoelectr.*, *45*, 1265–1274, 1993.

Kanasewich, E. R., *Time Sequence Analysis in Geophysics*, 364 pp., Univ. of Alberta Press, Edmonton, 1973.

Kaneshima, S., and G. Helffrich, Detection of lower mantle scatterers northeast of the Mariana subduction zone using short-period array data, *J. Geophys. Res.*, *103*, 4825–4838, 1998.

Kaneshima, S., and G. Helffrich, Dipping lower-velocity layer in the mid-lower mantle: Evidence for geochemical heterogeneity, *Science*, *283*, 1888–1891, 1999.

Kawakatsu, H., and F. Niu, Seismic evidence for a 920-km discontinuity in the mantle, *Nature*, *371*, 301–305, 1994.

Kellogg, L. H., B. H. Hager, and R. D. van der Hilst, Compositional stratification in the deep mantle, *Science*, *283*, 1881–1884, 1999.

Kendall, M., and P. G. Silver, Constraints from seismic anisotropy on the nature of the lowermost mantle, *Nature*, *381*, 409–412, 1996.

Kennett, B. L. N., and E. R. Engdahl, Travel times for global earthquake location and phase identification, *Geophys. J. Int.*, *105*, 429–465, 1991.

Kennett, B. L. N., E. R. Engdahl, and R. Buland, Constraints on seismic velocities in the Earth from travel times, *Geophys. J. Int.*, *122*, 108–124, 1995.

Kruger, F., M. Banumann, F. Scherbaum, and M. Weber, Mid mantle scatterers near the Mariana slab detected with a double array method, *Geophys. Res. Lett.*, *28*, 667–670, 2001.

Lay, T., Q. Williams, and E. J. Garnero, The core-mantle boundary layer and deep Earth dynamics, *Nature*, *392*, 461–468, 1998.

Matsuzawa, T., N. Umino, A. Hasegawa, and A. Takagi, Upper mantle velocity structure estimated from *PS*-converted waves beneath the north-eastern Japan arc, *Geophys. J. R. Astron. Soc.*, *86*, 767–787, 1986.

Mori, J., and D. V. Helmberger, Localized boundary layer below the mid-Pacific velocity anomaly identified from a *PcP* precursor, *J. Geophys. Res.*, *100*, 20,359–20,365, 1995.

Muirhead, K. J., Eliminating false alarms when detecting seismic events automatically, *Nature*, *217*, 533–534, 1968.

Niu, F., and H. Kawakatsu, Depth variation of the mid-mantle seismic discontinuity, *Geophys. Res. Lett.*, *24*, 429–432, 1997.

Niu, F., and L. Wen, Strong seismic scatterers near the core-mantle boundary west of Mexico, *Geophys. Res. Lett.*, *28*, 3557–3560, 2001.

Ohmi, S., and S. Hori, Seismic wave conversion near the upper boundary of the Pacific plate beneath the Kanto district, Japan, *Geophys. J. Int.*, *141*, 136–148, 2000.

Ohtani, E., M. Toma, K. Litasov, T. Kubo, and A. Suzuki, Stability of dense hydrous magnesium silicate phases and water storage capacity in the transition zone lower mantle, *Phys. Earth Planet. Inter.*, *124*, 105–117, 2001.

Ono, S., E. Ito, and T. Katsura, Mineralogy of subducted basaltic crust (MORB) from 25 to 37 GPa, and chemical heterogeneity of the lower mantle, *Earth Planet. Sci. Lett.*, *190*, 57–63, 2001.

Shieh, S. R., H. K. Mao, R. J. Hemley, and L. C. Ming, Decomposition of phase D in the lower mantle and the fate of dense hydrous silicates in subducting slabs, *Earth Planet. Sci. Lett.*, *159*, 13–23, 1998.

Sipkin, S. A., and M. D. Zirbes, Moment-tensor solutions estimated using optimal filter theory: Global seismicity, 1995, *Phys. Earth Planet. Inter.*, *101*, 291–301, 1997.

Tackley, P. J., Mantle convection and plate tectonics: Toward and integrated physical and chemical theory, *Science*, *288*, 2002–2007, 2000.

van der Hilst, R. D., and H. Karason, Compositional Heterogeneity in the bottom 1000 kilometers of Earth's mantle: Toward a hybrid convection model, *Science*, *283*, 1885–1888, 1999.

van der Hilst, R. D., S. Widiyantoro, and E. R. Engdahl, Evidence for deep mantle circulation from global tomography, *Nature*, *386*, 578–584, 1997.

Vidale, J. E., G. Schubert, and P. S. Earle, Unsuccessful initial search for a midmantle chemical boundary with seismic arrays, *Geophys. Res. Lett.*, *28*, 859–862, 2001.

Vinnik, L., F. Niu, and H. Kawakatsu, Broad-band converted phases from midmantle discontinuities; *Earth, Planets Space*, *50*, 987–990, 1998.

Vinnik, L., M. Kato, and H. Kawakatsu, Search for seismic discontinuities in the lower mantle, *Geophys. J. Int.*, *147*, 41–56, 2001.

Wen, L., Seismic evidence for a rapidly-varying compositional anomaly at the base of the Earth's mantle beneath the Indian Ocean, *Earth Planet. Sci. Lett.*, *194*, 83–95, 2001.

Widiyantoro, S., A. Gorbatov, B. L. N. Kennett, and Y. Fukao, Improving global shear wave traveltime tomography using three-dimensional ray tracing and iterative inversion, *Geophys. J. Int.*, *141*, 747–758, 2000.

Wiens, D. A., J. Hildebrand, and W. Crawford, Source and Aftershock Studies of the 1995 Marianas and 1996 Flores Sea Deep Earthquakes, *Eos Trans. AGU*, *77*(46), Fall Meet. Suppl., F491–F492, 1996.

Wysession, M. E., A. Langenhorst, M. J. Fouch, K. M. Fischer, G. I. Al-Eqabi, P. J. Shore, and T. J. Clarke, Lateral variations in compressional/shear velocities at the base of the mantle, *Science*, *284*, 120–125, 1999.

———————————

Y. Fukao and H. Kawakatsu, Earthquake Research Institute, University of Tokyo, 1-1-1 Yayoi, Bunkyo-ku, Tokyo 113, Japan. (fukao@eri.u-tokyo.ac.jp; hitosi@eri.u-tokyo.ac.jp)

F. Niu, Department of Earth Science, Rice University, 6100 Main Street, Houston, TX 77005, USA. (niu@rice.edu)